Proceedings of the 8th International Conference on Modeling and Simulation of
Metallurgical Processes in Steelmaking (STEELSIM 2019)
13–15 August 2019, Toronto, Ont., Canada
DOI 10.33313/503/068

Modeling of Transient Behavior of Top-Surface Slag/Molten Steel Interface in Continuous Slab Casting

Seong-Mook Cho and Brian G. Thomas

Department of Mechanical Engineering, Colorado School of Mines
1610 Illinois Street, Golden, Colorado 80401, USA
Phone: 303-273-3309
Email: seongmookcho1@mines.edu (Seong-Mook Cho) and bgthomas@mines.edu (Brian G. Thomas)

Keywords: LES, VOF, RANS, standard k-ε, surface instability, slag, entrainment, entrapment, slab mold

INTRODUCTION

Mold flux is added onto the surface of the molten steel pool in the mold during steel continuous casting to prevent reoxidation of the steel, to capture non-metallic inclusions, to insulate the surface from heat loss, and to lubricate the solidifying steel shell against the mold walls. However, unoptimized mold flow phenomena such as excessive surface velocity and surface level fluctuations can entrain the mold flux into the molten steel or may entrap slag into the steel shell [1], leading to slag defects in final steel products [2,3]. It is well known that slag defects may arise even during steady casting conditions, due to chaotic transient behavior at the mold flux/molten steel interface, such as sudden level drops [4]. Thus, it would be useful to improve understanding of transient flow behavior in this important region of continuous casting process.

Tools to quantify top-surface slag behavior in continuous casting include plant measurements [4-8], water model experiments [9-11], and computational modeling [4,9,12]. In particular, water-oil modeling is a useful and easy tool to qualitatively investigate mold flux/molten steel phenomena in continuous steel casting, due to the similar kinematic viscosities of water and molten steel. However, matching the important ratios of mold flux/molten steel properties including density, viscosity, and interface tension, which greatly influence interface behavior is difficult. Thus, computational models validated with plant data are a powerful methodology to quantitatively simulate and better understand these complex phenomena [13-16] and to suggest practical strategies to improve the operation and lessen the formation of slag defects.

This work applies computational modeling, plant measurements, and water model experiments to quantify transient behavior of the liquid mold flux/molten steel interface in continuous slab casting. This paper builds on previous studies [4,17] which have compared flow between the real caster, water models; and computational models. Finally, the validated computational model is applied to investigate the effects of nozzle port angle on mold flow, transient behavior of the mold flux/molten steel interface, and slag entrainment and entrapment in a typical slab-casting mold for typical casting conditions (Table 1).

© 2019 by the Association for Iron & Steel Technology.

Table 1. Caster dimension and process conditions

Caster dimensions	Real caster: R	1/3 scale water model: W
Nozzle bore inner diameter	D_{in}: 65 mm (at UTN top) to 60 mm (at bottom well)	D_{in}: 20.8 mm (average)
Nozzle bore outer diameter	D_{out}: 110 mm	D_{out}: 36.6 mm
Nozzle bottom well depth	d: 11 mm	d: 3.7 mm
Nozzle port width	60 mm	20 mm
Nozzle port height	Case R1: h: 65 mm, h': 67.3 mm Case R2: h: 65 mm, h': 75.1 mm	Case W1: h: 21.7 mm, h': 22.5 mm Case W3: h: 21.7 mm, h': 22.5 mm
Nozzle port angle	Case R1: θ : +15° (up), Case R2: θ: -30° (down)	Case W1: θ: +15° (up), Case W3: θ: -15° (down)
Nozzle length	1250 mm	416.7 mm
Area ratio between two ports and nozzle bore	2.54	
Mold width (W) / thickness (T)	1600 mm / 200 mm	533 mm / 67 mm
Aspect ratio between mold W and T	8	
Domain length	4780 mm (total); 2790 mm (mold and strand regions)	1994 mm (total); 1277 mm (mold and strand regions)
Process conditions		
Liquid flow rate	256 LPM (1.8 tonne/min)	16.4 LPM
Casting speed	0.8 m/min (13.3 mm/s)	0.5 m/min (8.3 mm/s)
Submerged depth of nozzle	140 mm	46.7 mm
Meniscus level below mold top	100 mm	33.3 mm
Average thickness of liquid mold flux layer on molten steel pool	L_{lm}: 10 mm	No slag layer
Gas injection	No gas	10 mL/min (0.06 % volume fraction for clear visualization of flows)

METHODOLOGY

Computational models of both the real caster and corresponding water model are applied to simulate the flow pattern and turbulence in the nozzle and mold, and the transient movement of the interface between the liquid mold flux and molten steel during nominally steady continuous slab casting. The model predictions are compared with plant measurements and / or one-third scale water-model experiments. Details of the models and measurements are given as follows.

Computational Modeling

Three-dimensional (3-D) finite-volume Computational Fluid Dynamics (CFD) models are used to simulate time-dependent and time–averaged flows in the nozzle and mold, and behavior of the interface between liquid mold flux and molten steel during steady continuous steel-slab casting. The models include a Large Eddy Simulation (LES) model [18] coupled with a Volume Of Fluid (VOF) model [19] for transient two-phase (molten steel-liquid mold flux) flow in the real caster and an Reynolds-Averaged Navier-Stokes equation (RANS) model with a standard k-ε model [20] for steady-state single-phase (molten steel or water) flow in the real caster or the water model. The equations for the models are solved using the finite volume method in ANSYS FLUENT [21].

LES coupled with VOF model

A LES model coupled with a VOF model is adopted to calculate transient molten-steel flow field and liquid mold flux/molten steel interface behavior in the mold region of a typical continuous steel-slab caster.

Mass conservation of the molten steel and the liquid mold flux phases together are satisfied using a single continuity equation. A single set of time-dependent momentum balance equations is solved for the two-phase mixture of molten steel and liquid mold flux considering interfacial tension between the two phases, calculated by the Continuum Surface Force model. The volume fraction of each phase is tracked with the VOF equation [19]. Mass and momentum sink terms are applied to cells next to the domain boundaries representing the steel shell to account for flow across the solidification front during solidification [22,23]. In this model, sink terms for the mold flux are not considered, because there is no slag consumption or solidification in the domain. These phenomena occur mainly outside of the domain. More details of the model equations are given in previous work [4].

The LES-VOF model adopts the full domain of a real caster, including part of the tundish bottom, the stopper-rod tip region, the entire Upper Tundish Nozzle (UTN), the entire Submerged Entry Nozzle (SEN) with nozzle ports, the top 3000 mm of the molten steel pool in the mold and strand, and a 10-mm thick layer of liquid mold flux layer at the mold top surface as shown in Figure 1. The SEN domain is connected with the mold domain and calculated together to obtain more accurate simulations of fluid flow in the mold [24]. The steel shell thickness profile down this caster is used to create the liquid domain, based on shell thickness measurements of a breakout shell at this caster. In order to achieve accurate flow calculations in the stopper region and below, the domain is extended upstream to include a cylindrical region of the tundish bottom around the stopper. The domain is meshed with over 4 million hexahedral cells: Case R1 with +15° (upward) ports and Case R2 with -30° (downward) ports, including 1mm cell length across the liquid mold flux layer and molten steel pool region near the interface between two phases.

© 2019 by the Association for Iron & Steel Technology.

Constant velocity is fixed as the inlet condition at the outside surface of a cylinder of fluid near the tundish bottom. This velocity (0.0014 m/sec) is calculated according to the molten steel flow rate and the surface area (0.982 m^2) of the cylindrical region. A pressure outlet condition is chosen on the domain bottom at the mold exit as 117 kPa gauge pressure considering the ferrostatic pressure due to the head of molten steel. The interface at the top surface wall (interface between the liquid mold flux and the sintered mold flux) is given a no-slip condition, which reflects that the sintered mold flux has much higher dynamic viscosity [25-27]. The domain walls representing the interface between the molten steel fluid and the solid steel shell is given a no-slip wall condition to move downward at the casting speed.

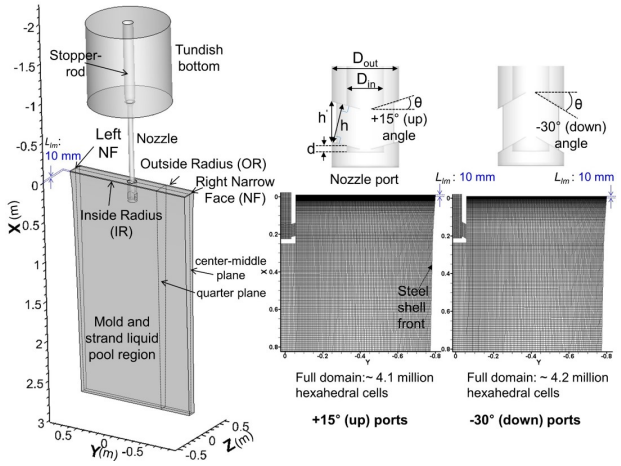

Figure 1. Domain and mesh of LES-VOF simulations of real caster.

RANS based standard k-ε model

The steady RANS equations with the standard k - ε model, a faster CFD model than the LES-VOF model, are solved for the time-averaged single-phase (molten steel or water) turbulent flow pattern in the nozzle and mold for both the real caster case (upward port-angle Case R1 with the same process conditions used in the LES-VOF simulations) and the water model cases (Cases W1 and W3). The RANS model uses a one-quarter domain (adopting 2-fold symmetry) without the slag layer, which consists of a structured mesh of 0.3 million hexahedral cells (real caster) and 0.15 hexahedral cells (water model).

For the real caster case, the same boundary conditions considered for the LES-VOF simulations are applied for the k - ε model, including the mass and momentum sink terms to account for solidification, except for additional conditions on *k* and ε. Specifically, small levels of turbulent kinetic energy ($10^{-5} m^2/s^2$) and turbulent kinetic energy dissipation rate ($10^{-5} m^2/s^3$) are set at the inlet surface of the tundish-bottom region, and for back flow entering the domain outlet. The no slip condition at the top surface, representing the liquid mold flux/molten steel interface is used for the real caster case, considering the ~30× higher dynamic viscosity of the liquid mold flux compared to the molten steel. For the water model cases, the boundary conditions corresponding to the water model conditions (Table 1) are applied. The top surface at the air/water interface is given by a stationary wall with 0 Pa shear stress components for free-slip boundary condition. During solving the equations, convergence is defined when all scaled residuals are stably reduced below 10^{-4}, for both the real caster and the water model cases.

Velocity fluctuations with the RANS model simulations are calculated from the turbulent kinetic energy *k*, assuming isotropic behavior as follows:

$$\text{RMS of } u_x' = \text{RMS of } u_y' = \text{RMS of } u_z' = \sqrt{\overline{(u_i')^2}} = \sqrt{\frac{2}{3}k} \quad [1]$$

Plant Measurements

Surface velocity and interface between liquid mold flux and molten steel are measured in the real caster using nail dipping tests and oscillation-mark profile measurements.

Nail dipping tests

Nail dipping tests are conducted to quantify surface velocity near the interface between liquid mold flux and molten steel in the mold during steady continuous casting. Five pairs of 5mm-diameter, 290 mm-long stainless steel nails, spaced 100 mm

© 2019 by the Association for Iron & Steel Technology.

apart, are dipped for 3 seconds at two-minute intervals, at 200 mm from the narrow face, as shown in Figure 2(a). The solidified lump on each nail is measured for lump diameter, φ_{lump} (mm) and lump height difference, h_{lump} (mm), as shown in Figure 2(a), and those two measured values are used to estimate velocity magnitude according to the empirical equation found and validated in previous work [8]. From the resulting histories of velocity magnitude and flow direction, the time average and variations of each velocity component are evaluated to validate the model predictions of the real caster.

Oscillation-mark profile measurements

Oscillation marks are small transverse depressions around the surface of steel slabs, produced by freezing and partial overflow of the molten steel over the meniscus during each mold oscillation cycle. Thus, each mark captures the instantaneous shape of the interface between the liquid mold flux and molten steel around the mold perimeter. In this work, the narrow face of the slab sample, including 10 oscillation marks, is sand blasted to reveal the surface, as shown in Figure 2(b). The oscillation mark lines are traced and graphed, maintaining total area under each curve of zero. These lines reveal variations of the liquid mold flux/molten steel interface profiles, which are used to validate the computational model predictions of the real caster.

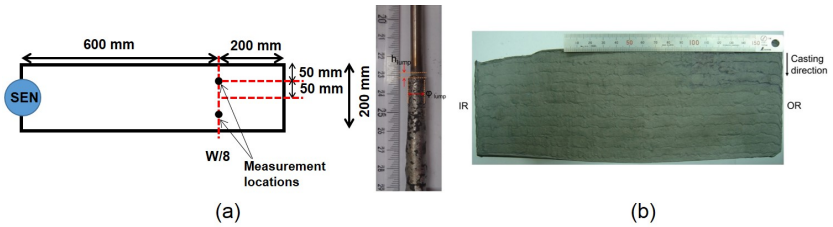

Figure 2. Plant measurements: (a) nail dipping tests and (b) oscillation-mark profile measurements.

Water Model Experiments

A one-third scale water model of the real continuous caster (Figure 3) is constructed to study nozzle and mold flow in this caster. The water model includes half of the tundish, the stopper-rod, the Submerged Entry Nozzle (SEN), and the mold region of the liquid pool in the strand. The water flow rate from the tundish through the SEN into the mold is controlled by changing the size of the annular gap between the stopper head and the bottom of the tundish. Water exits holes in the mold bottom to a holding water bath, and then is pumped continuously back up to the tundish. Two different nozzle ports are investigated in this study of the effect of port angle on the mold surface flow. Both nozzles are bifurcated with typical rectangular ports, differing only regarding the angle of the ports. Table 1 provides details of the casting conditions and caster dimensions, comparing the real caster and the 1/3 scale water model. Casting speed in the water model is chosen based on maintaining a constant Froude number, which is defined as the ratio of inertia force to gravitational force ($V/\sqrt{gL}$).

Measurements of instantaneous surface velocity are performed using an electromagnetic current sensor located at three positions: 10mm from the free surface in the water model (W: mold width): 1) 30mm from Narrow Face (NF), 2) W/8, 3) W/4 positions on the left NF. Instantaneous horizontal velocity data is collected every 0.1 s for 1000 s. The sensor measures two components of horizontal surface velocity: one towards the NF, and the other (cross flow) towards to the WF. In addition, dye and a small amount (0.06 % volume flow-rate fraction of gas in the water) are injected to visualize the flow. Flow is recorded with three video cameras to provide a NF end view, surface bottom view, and Wide Face (WF) front view.

© 2019 by the Association for Iron & Steel Technology.

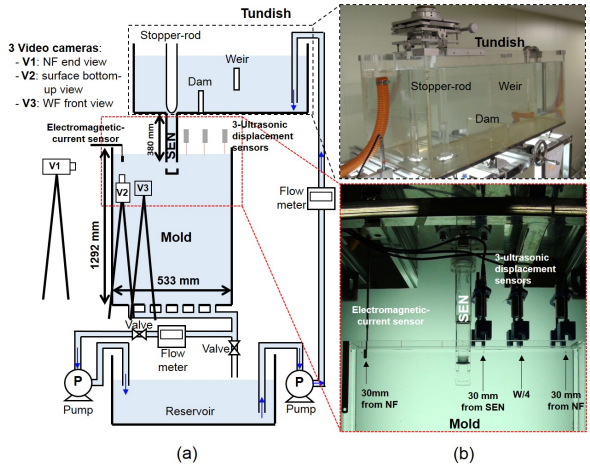

Figure 3. 1/3-scale water model: (a) schematic and (b) photos.

RESULTS AND DISCUSSION

Flow results are first compared for: real caster VS. water model and LES-VOF model VS. RANS based k-ε model. Then, the LES-VOF model validated with plant measurements is applied to quantify the effects of nozzle port angle on mold flow, top surface slag/molten steel interface behavior, and slag entrainment and entrapment in the real caster.

Comparison of Flows between Real Caster and Water Model

Previous works have shown that single-phase flow in water models generally matches that in commercial casters, except near the top surface, due to the effects of the slag layer, and in thin-slab casters, due to upward deflection of the jet by the solidifying steel shell, which takes up a significant fraction of the thickness cross section in the mold region [28,29].

In this work, both the computational model predictions of the real caster and the plant measurements show a single-roll flow pattern for the upward-ports case (Case R1), as shown in Figures 4(a) and 5(a). This contrasts with results from a 1/3-scale water model for the exact same conditions (Case W1), in which both the water-model measurements and RANS simulations show a double-roll flow pattern, as shown in Figures 4(b) and 5(b). All results for both cases agree that surface velocities are higher with downward ports, but surface level fluctuations and turbulence are higher with upward ports, as shown in Figure 5.

This finding that the flow pattern in the water model is opposite from that observed in the plant measurements may be explained by two reasons. Besides the scale factor and minor differences in fluid properties, the only differences are neglect of 1) the slag layers and 2) the solidifying steel shell. Although the effect of the curved shape of the solidifying shell walls is usually small in a thick-slab caster, its effect on causing upward deflection is apparently enough to change the flow pattern in this case. This is likely because the jet from the upward ports of this nozzle spreads to impinge strongly onto the wide faces, so can be deflected further upwards, and because the flow pattern for this case is somewhat unstable and near to changing directions. Perhaps the free surface movement of the water model contributed as well.

It should be emphasized that the simulations match well with the measurements for both the real caster and water model cases. For the real caster case, the LES-VOF and the RANS models both predict the single-roll pattern measured in the plant case. The RANS model matched well with the double-roll pattern in the water model case. These findings reveal that computational modeling is an ideal tool to quantify complex flow in continuous casting.

© 2019 by the Association for Iron & Steel Technology.

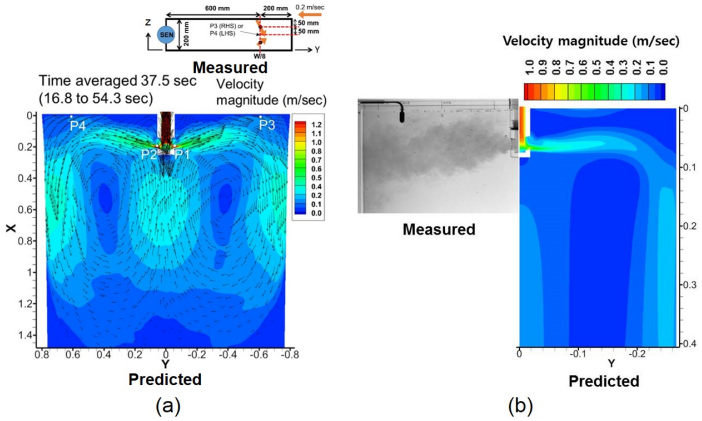

Figure 4. Mold flow pattern, comparing (a) real caster and (b) 1/3-scale water model.

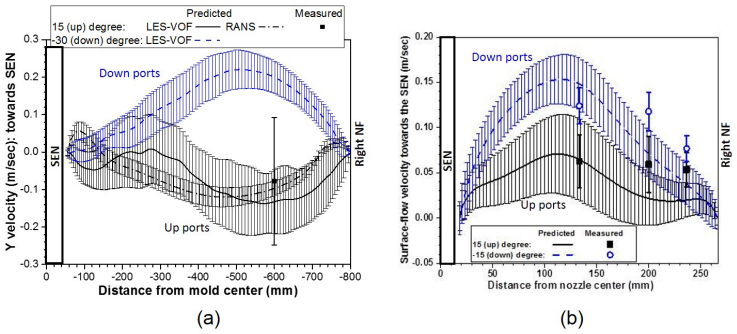

Figure 5. Comparison of surface velocity between (a) real caster and (b) water model.

Comparison of Flow Prediction between LES-VOF Model and RANS Based Standard k-ε Model

The nozzle swirl phenomena predicted by the LES-VOF model match well with those observed in the water model experiments, as shown in Figure 6. The swirl fills the entire port and alternates between clockwise and counter-clockwise directions. However, the steady-state RANS model predicts smaller swirl region area than is measured, due to the quarter domain of the RANS model [17]. Thus, the LES model with no symmetry assumption is beneficial for realistic capture of the transient swirl behavior in the nozzle.

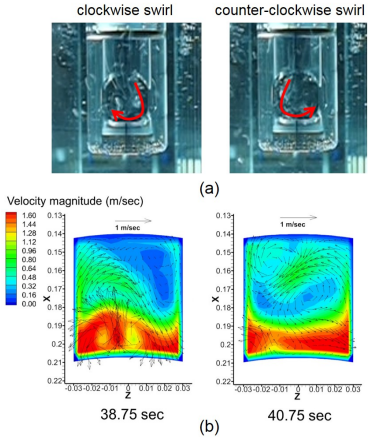

Figure 6. Transient swirl at nozzle port exit with +15° (up angle), comparing (a) water model experiments and (b) LES-VOF simulations of real caster.

The predicted horizontal surface velocity components (Y velocity: towards SEN, Z velocity: toward OR) and their fluctuations are compared with the measurements from the nail dipping tests in Figures 7(a) and 7(b). Both the LES and

© 2019 by the Association for Iron & Steel Technology.

RANS models reasonably match with the time-averages of the measured velocity profiles. However, the LES-VOF model better captures the high magnitude of the real fluctuations at the mold surface, represented by the error bars. This is likely because the RANS model predictions of turbulent fluctuations near the interface are deficient, because velocity variations across the symmetry planes are suppressed, including both crossflow between WFs and sloshing between NFs.

To compare the liquid mold flux/molten steel profiles predicted from the LES-VOF simulation with the single-phase RAN modeling, time-averaged surface level profile, h_i is calculated from static pressure distribution predicted using the RANS model, as follows [5].

$$h_i = \frac{P_i - P_{avg}}{[\rho_s - (1-c)\rho_f]g} \quad [2]$$

where P_i is static pressure at location i, P_{avg} is spatial-averaged pressure across the mold surface, and c is a constant to quantify the extent of slag displacement due to density differences relative to vertical motion (ie lifting) of the slag/molten steel interface. Assuming the constant c=0 means that slag motion is caused only by displacement of slag by molten steel, as gravity causes some slag to flow down to where the steel level profile is lower and away from where the steel level is higher. A constant of c=1 means that the slag is simply lifted up and down by the local steel level motion, with no change in the liquid-slag layer thickness. This constant was previously quantified as an empirical coefficient to match plant measurements [6]. Figure 7(c) shows predicted interface profiles across the mold surface from the RANS and the LES-VOF simulations. The surface level profiles all generally agree, except for the slight hump in the LES-VOF profile at ~400 mm, where the jet flow impinges, which is not captured by the RANS models. This is a natural consequence of the flow pattern differences. The RANS models also miss the sharp level drops at the meniscus regions, due to their neglect of surface tension. The RANS model with the slag-displacement model (c=0) shows better agreement with the LES-VOF model, with a steeper slope from SEN to right NF. Considering that the LES model should be more accurate, and agrees better with plant measurements [5,6], this finding appears to contrast with previous work that showed better agreement with the slag-lifting model. This is explained however, as vertical lifting of the liquid slag layer, such as during relatively rapid level fluctuations measured in previous work [5,6] occurs in short time scales, while longer times, of greater interest in this work, are likely needed to enable the slow-flowing slag to develop significant slag displacement.

Thus, the LES-VOF model is more accurate and useful to simulate transient fluid flow and the interface between liquid mold flux and molten steel, which are more strongly related to slag defect formation mechanisms.

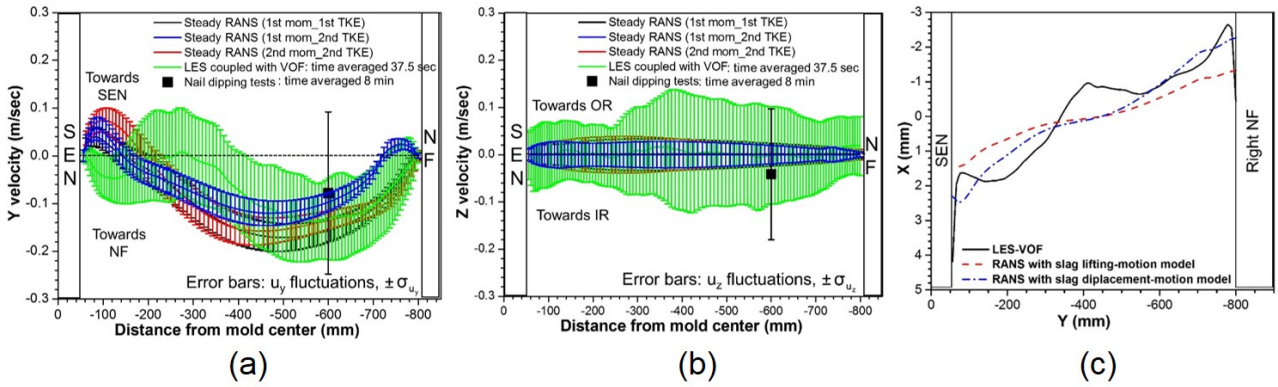

Figure 7. Comparison of (a) horizontal surface-flow velocity, (b) cross surface-flow velocity, and (c) surface level profile comparing LES-VOF and RANS model predictions of real caster.

Effect of Nozzle Port Angle: Real Caster Cases

Two nozzle-port angle cases (Cases R1 and R2) are studied to quantify effects of the port angle on mold flow, liquid mold flux/molten steel interface motion, and slag entrainment and entrapment during continuous steel-slab casting. The LES-VOF model validated via nail board dipping tests and oscillation mark profile measurements is used.

© 2019 by the Association for Iron & Steel Technology.

Mold flow

Jet flows into the mold generate very different flow patterns with the two different port angles. The upward-ports case produces a single-roll flow pattern, as the high-spreading jet impinges first onto the wide faces, and deflects upwards to impinge into the mold top surface, midway between the SEN and the NF, as shown in Figure 8(a). The downward-ports case generates a classic double-roll flow pattern, where the less-spreading jet impinges first onto the narrow face, and splits to send flow up the narrow face towards the top surface, as shown in Figure 8(b). In addition, jet wobbling is more severe with upward ports, compared to downward ports. This corresponds to higher TKE of the jet in the mold with the upward ports, in addition to higher TKE at the surface, compared with the stable double roll flow pattern with the downward ports, as shown in the bottom-frames of Figure 8.

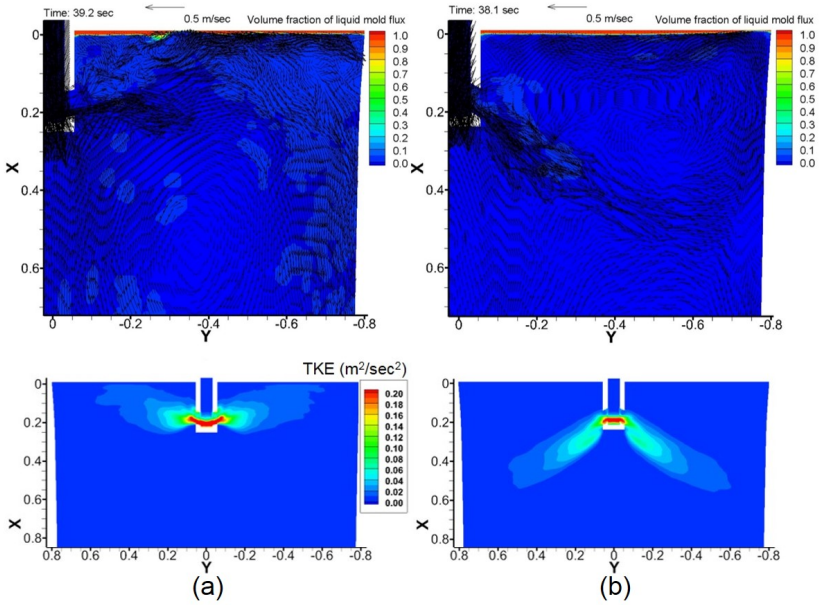

Figure 8. Instantaneous mold flow pattern, slag/steel interface behavior, and TKE at center-middle plane in the mold, comparing (a) + 15 deg (up) ports and (b) 30 deg (down) ports.

Simulated histories of the surface velocity at the measured location (at both symmetrical points P3 and P4) are compared for both cases in Figure 9. In addition to matching the measured trends, the predictions generally fall within the quantitative range of the measurements, and the time-means agree reasonably as well.

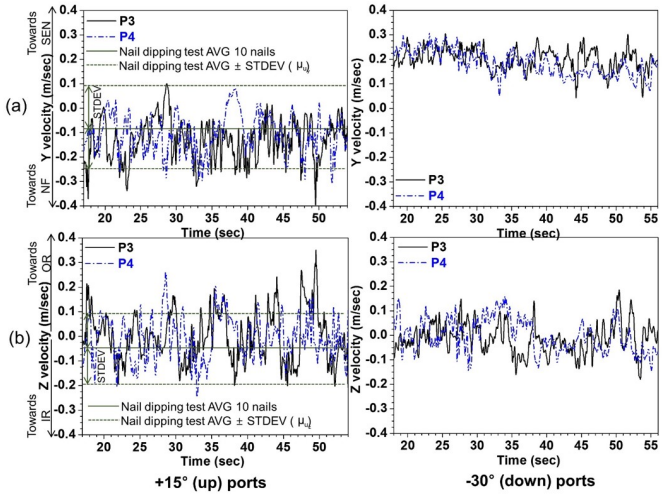

Figure. 9. Comparison of surface velocity histories (at points P3 and P4) between simulations and measurements for upward and downward nozzles: (a) y velocity (horizontal velocity) and (b) z velocity (cross velocity).

© 2019 by the Association for Iron & Steel Technology.

Liquid mold flux/molten steel interface motion

Nozzle port angle greatly affects the profile of the interface between the liquid mold flux and the molten steel and its time variations. Figure 10 shows the time-averaged meniscus level profiles (slag/steel interface) on three wide face views (upper frames) and four narrow face views (lower frames) for each port-angle case. In these frames, zero represents the time and spatial average of the meniscus level, which is 10mm below the top of the initial liquid layer.

The meniscus level profiles for both nozzle angles show strong curvature, contacting the walls at the inner radius, IR, and outer radius, OR, ~3 mm lower than the farfield surface level, due surface tension. This is why the IR and OR surface profiles are generally so much lower than the center section. This meniscus curvature is most obvious at the center plane between the narrow faces, in the thin channels between the SEN and wide faces. Here, the surface tension suppresses the liquid level by over 4 mm. Meniscus curvature is greatest in the corners, which agrees with previous studies [30], and confirms that the current LES-VOF model can make realistic predictions of meniscus shape. With upward ports, the highest surface level is found at the quarter-plane location, where the jet flow impinges to make a hump. The hump is more severe near the meniscus on both the IR and OR walls, due to strong upward flow from jet impingement on the wide faces in this region. Surface level also builds up towards the narrow faces, as jet flow with this nozzle is strong from the hump to the narrow faces.

On the other hand, the interface profile experiences a trough (minimum level) between the SEN and narrow face with the downward ports, where surface velocity is highest. High crests are produced near the narrow faces, where the strong upward flow impinges upon the meniscus region. The maximum average difference of surface level from crest to trough is ~8 mm with this nozzle, which is even higher than the ~6 mm maximum profile variation observed with upward ports, due to the generally higher surface velocities associated with the classic double roll pattern with downward ports.

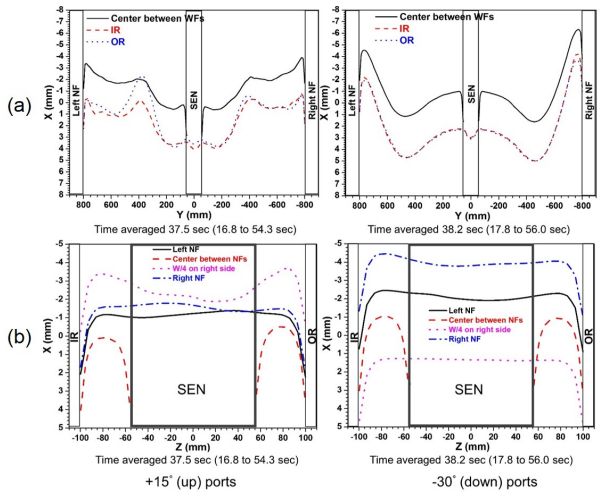

Figure 10. Comparison of time-averaged slag/steel interface profile (liquid mold flux volume fraction: 0.5) on (a) wide face view (front view) and (b)narrow face view (side view) in the mold comparing cases with upward and downward ports.

Surface level fluctuations, vertical variations of the slag/molten steel interface with time, are shown for both nozzles in Figure 11(a) as σ_x, standard deviations of the level at the center-middle plane and IR meniscus. The level fluctuations are generally more severe with upward ports than with downward ports, especially at the meniscus region (IR), as also shown in Figure 11(b). With upward ports, the maximum average level fluctuations are 3.4 mm (within one standard deviation), found roughly midway between SEN and NF, due to unstable wobbling of the jet where it impinges the top surface.

With downward ports, the maximum level fluctuations are only 2.3 mm, found at the meniscus on the right NF, due to asymmetric mold flow causing variations in the vertical momentum up the narrow faces, which indicates slight sloshing behavior at very low frequency (> 18 s time period).

© 2019 by the Association for Iron & Steel Technology.

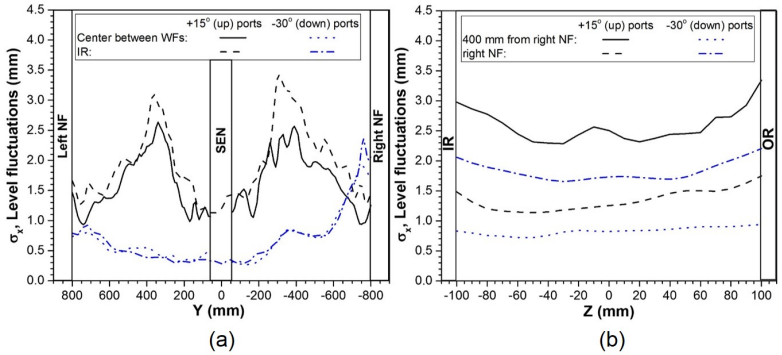

Figure 11. Comparison of level fluctuations of slag/steel interface (liquid mold flux volume fraction: 0.5) on (a) wide face view (front view) and (b) narrow face view (side view) comparing cases with upward and downward ports.

Time-average and fluctuations (standard deviations) of the slag/molten steel interface level at the meniscus simulated at the right narrow face for downward ports are compared in Figure 12 with five oscillation mark profiles measured on the steel slab (Figure 2(b)). The predicted meniscus level, including both the time average (red dash-dot line) and fluctuations (red error bars), agree reasonably well with the measurements (black solid lines). Both the simulation and measurements show reasonably horizontal profiles, with variations of ±2 mm, except near the corners, where the levels dip down much further, as explained previously. This further validates the LES-VOF model. The measured oscillation mark profiles in the corner region near the OR are consistently much lower than near the IR. In a similar manner, the simulated left NF profile is consistently lower than the right NF profile. This shows that asymmetric flow can persist for many oscillation cycles, producing regions of deeper oscillation marks which are fundamentally rooted in chaotic turbulent flow behavior.

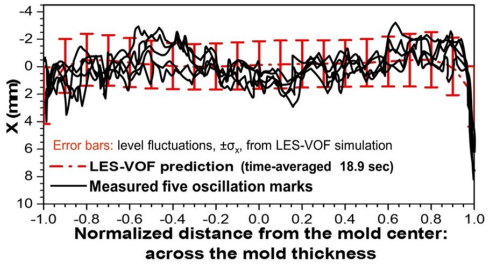

Figure 12. Comparison of the predicted meniscus profile with measured oscillation marks profiles on right narrow face for case with downward-angled nozzle ports.

Slag entrainment and entrapment

Turbulent steel flow at the slag-steel interface may push or drag the liquid mold flux via shear, leading to the entrainment of slag droplets into the flowing steel. The flow also may cause sudden level fluctuations, leading to slag entrapment into the solidifying steel shell, if the fluctuations occur near the meniscus. Other entrained slag droplets in the molten steel pool may become entrapped into the solidifying steel shell, after they are transported through the turbulent flowing steel, contact the shell, and satisfy the capture criterion. The remaining entrained droplets are absorbed safely back into the slag layer. Increased surface velocity increases the possibility of slag entrainment via the upward flow mechanism [31], and shear layer instability [32-34]. Figure 13 shows time variations of surface velocity magnitude (at P3 and P4) with critical surface velocities based on these slag entrainment mechanisms for both the upward and downward ports. Average velocity magnitude with the downward ports is higher than with the upward ports. However, the results showing mean velocity are less than the thresholds for slag entrainment, so chronic entrainment problems are not expected from either nozzle.

© 2019 by the Association for Iron & Steel Technology.

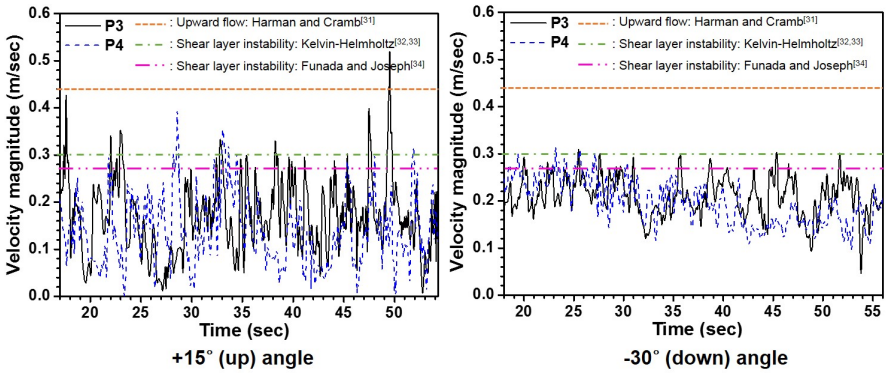

Figure 13. Comparison of predicted surface velocity magnitude (at points P3 and P4) with slag entrainment criterions for cases with (a) upward ports and (b) downward ports.

Figure 14(a) shows details of the slag entrapment mechanism with level fluctuations. A severe level drop brings the liquid slag into contact with the steel solidification front, where it may become finally entrapped just beneath the surface of the steel shell. Such entrapped slag can cause surface defects, such as shown in Figure 14(b) if the thickness of the surface layer removed by scale formation and expensive subsequent scarfing or grinding operations is insufficient. This entrapment mechanism is particularly problematic for stainless steels, because surface oxidation is so small. Previous plant guidelines for grinding depth have been based on removing a surface layer equal to the maximum hook depth [35]. Based on the level-drop mechanism in Figure 14(a), a criterion for critical level drop, h_{cr} which may lead to slag defects can be estimated as follows

$$h_{cr} = u_{casting}\left(\frac{L_g}{k_c}\right)^2 \qquad [3]$$

where $u_{casting}$ is casting speed, L_g is grinding thickness, and k_c is an empirical coefficient to estimate the solidifying steel shell thickness along the casting direction. This equation suggests that higher casting speed, larger grinding thickness, and slower shell growth rate all increase the critical level drop, which should lessen slag defects based on this mechanism. For the current casting conditions, with 1.5 mm of surface thickness removed by grinding the wide faces, the critical level drop is 2.6 mm (WF) and 0 mm (NF). Figure 14(c) shows average meniscus level, critical surface level, and instantaneous level profiles on both IR and right NF. Five potential instances of slag entrapment are observed in just this single snapshot, which confirms the importance of this mechanism. Figure 15 compares the instantaneous distribution of slag at the IR steel shell front between upward and downward ports, which involves very small volume-fraction contours. The mold cavity for the upward port case is seen to contain much more slag, due to both more entrainment and more entrapment near the meniscus. This work agrees with and explains the plant experience that more surface defects related to mold slag entrapment are found with the SEN with upward ports.

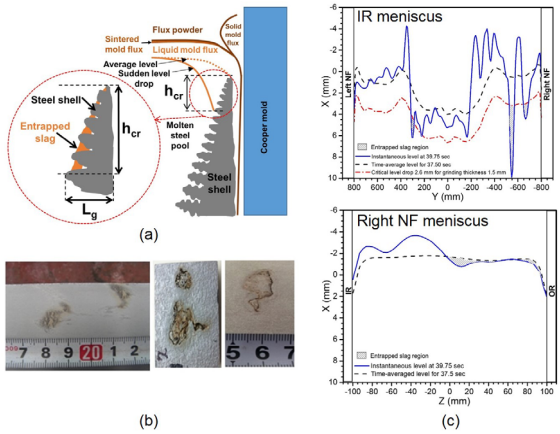

Figure 14. Slag entrapment near meniscus with + 15 deg (up) angled nozzle ports: (a) schematic of mechanism, (b) surface defect caused by slag entrapment, and (c) predicted slag entrapment into solidifying steel shell.

© 2019 by the Association for Iron & Steel Technology.

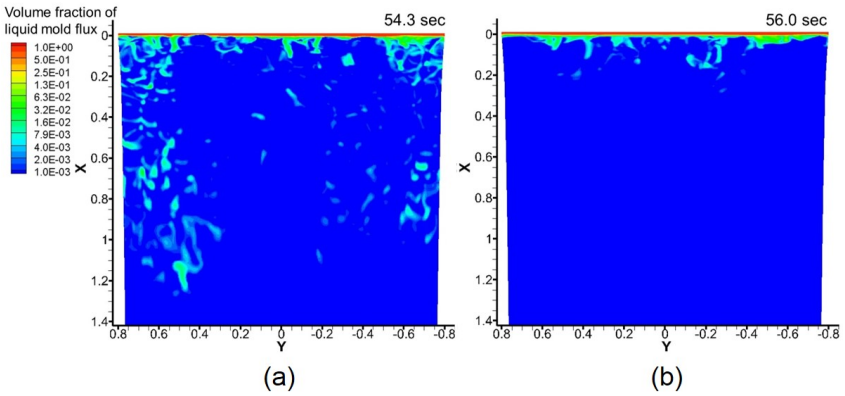

Figure 15. Instantaneous slag distribution at IR steel shell front for LES cases with (a) upward ports and (b) downward ports.

SUMMARY AND CONCLUSIONS

This work applies three-dimensional CFD models, commercial plant measurements, and 1/3-scale water model experiments to quantify turbulent molten-steel flow and behavior of liquid mold flux/molten steel interface in a typical continuous steel-slab caster under nominally-steady conditions. Findings regarding modeling include:

1. Both measurements and RANS simulations of the water model show a double-roll flow pattern, which differs from flow in the real caster for the upward ports case, in which both measurements and models show a single-roll flow pattern. This is likely due to the water model missing the solidifying steel shell and the top surface slag layer. This finding shows both the dangers of water modeling, and the potential benefits of computational models.
2. The RANS-based flow model can reasonably predict time-averaged flow and surface velocity magnitude. However, surface flow impingement and velocity fluctuations are underpredicted (relative to the LES model), due to the RANS model inability to capture asymmetric flow between sides of the caster.
3. The LES-VOF model shows reasonable agreement with plant measurements of surface velocity from nail dipping tests and meniscus level profiles from oscillation mark profile measurements. The simple slag-displacement model based on surface pressure variations compares well with the full LES -VOF model results.

Next, the effects of nozzle port angle on mold flow, liquid mold flux/molten steel interface motion, and slag entrainment and entrapment are investigated using the validated LES-VOF model, under nominally-steady conditions. Findings include:

1. Jet flow from upward-angled nozzle ports produces a single-roll pattern with jet impingement on the top surface midway between the SEN and NF, where the highest surface level and greatest level fluctuations are produced. Larger momentum diffusion with a broader jet across the mold thickness results in slightly lower surface velocities and a flatter surface profile, compared to the nozzle with downward-angled ports.
2. The downward ports generate a classic double-roll flow pattern with a strong, high-momentum jet and flow p the narrow faces that impinges on the narrow face meniscus, where it produces a crest in the level profile and maximum in level fluctuations. The highest surface velocity is across the center region, midway between the SEN and NF, where it produces a trough in surface profile.
3. The single-roll flow pattern from the upward ports leads to severe surface level fluctuations, due to strong variations in surface cross flow velocity between WFs. Sudden severe level drops of over ~10 mm are generated, which likely increase the chances of slag entrapment into the initial solidifying steel shell, especially on the WFs near the quarter plane. Results from a new model based on entrapped slag depth corresponding with level drops, suggest that 1.5 mm of grinding would not be sufficient to remove surface slag for the stainless steel slabs and casting conditions investigated here. Thus, deeper submergence is suggested for upward-angled nozzle ports with the current casting conditions, in order to generate a more stable double-roll pattern.

ACKNOWLEDGEMENTS

The authors thank Seon-Hyo Kim, Hyoung-Jun Lee, Dae-Woo Yoon, POSTECH for help with the 1/3 scale water model experiments, and Shin-Eon Kang, POSCO Technical Research Laboratories for providing the water model. Support from the Continuous Casting Center at Colorado School of Mines, the Continuous Casting Consortium at University of Illinois at Urbana-Champaign, POSCO, South Korea (Grant No. 4.0011721.01), and the National Science Foundation GOALI grant

© 2019 by the Association for Iron & Steel Technology.

(Grant No. CMMI 18-08731) are gratefully acknowledged. Provision of FLUENT licenses through the ANSYS Inc. academic partnership program is also much appreciated. This research is part of the Blue Waters sustained-petascale computing project, which is supported by the National Science Foundation (awards OCI-0725070 and ACI-1238993) and the state of Illinois. Blue Waters is a joint effort of the University of Illinois at Urbana-Champaign and its National Center for Supercomputing Applications.

REFERENCES

1. L.C. Hibbeler and B. G. Thomas, *Iron Steel Technol.*, 2013, Vol. 10(10), pp. 121-136.
2. C. Ojeda, B. G. Thomas, J. Barco, and J. L. Arana: *Proc. of AISTech 2007*, Assoc. Iron Steel Technology, Warrendale, PA, USA, 2007, vol. 1, pp. 269-284.
3. J. Sengupta, C. Ojeda, and B. G. Thomas: *Int. J. Cast Met. Res.*, 2009, vol. 22, pp. 8-14.
4. S-M. Cho, B. G. Thomas, and S-H. Kim, *Metallurgical and Materials Transactions B*, 2019, Vol. 50(B), pp. 52-76.
5. S-M. Cho, B. G. Thomas, and S-H. Kim, *Metallurgical and Materials Transactions B*, 2016, Vol. 47(B), pp. 3080-3098.
6. S-M. Cho, S-H. Kim, and B. G. Thomas, *ISIJ Int.*, 2014, Vol. 54, No. 4, pp.855-864.
7. C. Ji, J. Li, H. Tang, and S. Yang, *Steel Research Int.*, 2013, Vol. 84, pp. 259-268.
8. R. Liu, B. G. Thomas, J. Sengupta, S. D. Chung and M. Trinh, *ISIJ Int.*, 2014, Vol. 54, pp. 2314-2323.
9. Z. Liu, Z. Sun, and B. Li, *Metallurgical and Materials Transactions B*, 2018, Vol. 48B, pp. 1248-1267.
10. R. Hagemann, R. Schwarze, H. P. Heller, and P. R. Scheller, *Metallurgical and Materials Transactions B*, 2013, Vol. 44B, pp. 80-90.
11. L. Campos, S. Vincent, J-P. Caltagirone, and P. Gardin, *8th International Conference on Computational and Experimental Methods in Multiphase and Complex Flow*, Valencia, Spain, April 20-22, 2015.
12. K. E. Swartz, L. C. Hibbeler, B. P. Joyce, and B. G. Thomas, *Iron and Steel Technology*, Vol.12 (7), July, 2015.
13. B. G. Thomas, *Steel Research Int.*, 2018, Vol. 89, 1700312.
14. B. G. Thomas, *Chapter 5. Modeling of Continuous Casting in Making, Shaping and Treating of Steel*, 11th ed., Cramb, A., ed.; AISE Steel Foundation: Pittsburgh, PA., USA, 2003; Volume 5, Casting Volume, pp. 5.1-5.24.
15. B. G. Thomas and L. Zhang, *ISIJ Int*., 2001, Vol. 41, pp. 1181–1193.
16. Q. Yuan, B. Zhao, S. P. Vanka, B. G. Thomas, *Steel Research Int*. 2005, Vol. 76, pp. 33-43.
17. S-M. Cho, B. G. Thomas, H-J. Lee, and S-H. Kim, *Iron and Steel Technology*, 2017, Vol. 14, No. 7, pp. 76-84.
18. F. Nicoud and F. Ducros, *Flow, Turbulence and Combustion* **1999**, Vol. *62*, pp. 183-200.
19. C. W. Hirt and B. D. Nichols, J. Comput. Phys., 1981, Vol. 39, p. 201.
20. B. E. Launder, D. B. Spalding, *Lectures in Mathematical Models of Turbulence*, Academic Press, London, England, 1972.
21. ANSYS FLUENT 14.5-Theory Guide, ANSYS. Inc., Canonsburg, PA, USA, 2012.
22. Q. Yuan, B. G. Thomas, and S. P. Vanka: *Metall. Mater. Trans. B*, 2004, vol. 35B, pp. 685-702.
23. R. Liu: Ph. D. Thesis, University of Illinois at Urbana-Champaign, 2015.
24. L. Zhang, Y. Wang, and X. Zuo, Metall. Mater. Trans. B, 2008, Vol. 39B, pp.534-550
25. B. Zhao, S. P. Vanka, and B. G. Thomas: *Int. J. Heat Fluid Flow*, 2005, vol. 26, pp. 105-118.
26. R. M. McDavid and B. G. Thomas: *Metall. Mater. Trans. B*, 1996, vol. 27B, pp. 672-685.
27. B. Xie, J. Wu, and Y. Gan: Proc. of Steelmaking Conference, ISS-AIME, Warrendale, PA, USA, 1991, pp. 647-651.
28. R. Chaudhary, B. T. Rietow, and B. G. Thomas, Proc. *Materials Science and Technology (MS&T)*, AIST/TMS, Pittsburgh, PA, 2009, pp. 1090-1101.
29. X. Jin, D. Chen, X. Xie, J. Shen, and M. Long, *Steel Res. Int*., 2013, Vol. 84, pp. 31-39.

© 2019 by the Association for Iron & Steel Technology.

30. G-G. Lee, B. G. Thomas, S-H. Kim, H-J. Shin, S-K. Baek, C-H. Choi, D-S. Kim, and S-J. Yu, *Acta Mater.*, 2007, Vol. 55, pp. 6705-6712.

31. J. M. Harman and A. W. Cramb, *Proc. 79th Steelmaking Conf.*, The Iron and Steel Society, Warrendale, PA, USA, 1996, pp. 773-784.

32. H. L. F. Von Helmholtz, Monatsb. K. Preuss. Akad. Wiss. Berlin, 1868, Vol. 23, pp. 215-228.

33. W. Thomson. (Lord Kelvin), *Phil. Mag.*, 1871, Vol. 42, No. 281, pp. 362-377.

34. T. Funada and D. D. Joseph, *J. Fluid*, 2001, Vol. 445, pp. 263-283.

35. H-J Shin, B. G. Thomas, G-G. Lee, J-M. Park, C-H. Lee, and S-H. Kim, *Proc. Materials Science and Technology (MS&T)*, Assoc. Iron Steel Technology, Warrendale, PA, USA, 2004, Vol. II, pp. 11-26.

© 2019 by the Association for Iron & Steel Technology.